International Journal of Heat and Mass Transfer 187 (2022) 122565

Contents lists available at ScienceDirect

International Journal of Heat and Mass Transfer

journal homepage: www.elsevier.com/locate/hmt

In-situ thermal analysis of intermetallic and thermite projectiles in high velocity impact experiments

Connor Woodruff[a], Steven W. Dean[b], Colton Cagle[a], Charles Luke Croessmann[a], Pascal Dubé[c], Michelle L. Pantoya[a,*]

[a] Mechanical Engineering Department, Texas Tech University, Lubbock, TX 79404-1021, USA
[b] Sandia National Laboratories, Albuquerque, NM, 87123, USA
[c] MATSYS, Inc., Sterling, VA 20164, USA

ARTICLE INFO

Article history:
Received 30 September 2021
Revised 4 January 2022
Accepted 9 January 2022

Keywords:
Pyrometry
Thermography
Aluminum
Flame temperature
Impact ignition
Fragmentation

ABSTRACT

Particle fragmentation influences thermochemical energy conversion processes in different ways and is of significance in energy generation technologies. Different reactive material formulations trigger varied thermal response in extreme environments such as high velocity impact. This study investigated optical thermal response of powder gun launched intermetallic (Al:Zr) and thermite (Al:MoO_3) projectiles using pyrometry and thermography. Projectiles were launched at 1250 m/s into an air-filled chamber and impacted a steel witness plate to create a dust explosion. The pyrometer was configured to measure temperatures directly at the point of impact, while the thermographic system measured temperatures throughout the explosion chamber. Results show that impact temperatures ranged between 3500 and 4000 K, but that the dynamics of energy conversion were different for the intermetallic and thermite projectiles. The intermetallic exhibited secondary reactions due to fragmented debris impacting the walls of the chamber. The thermite exhibited greater gas generation, propelling the debris field, and producing a more stochastic response with faster spreading and dissipation of thermal energy. Unique features such as microexplosions within fragmented particles were also analyzed. While both reactive materials produce similar temperatures, their mechanisms of energy conversion and release are different, indicating the potential of these materials for different ballistic applications.

1. Introduction

Reactive materials are solid compositions of two or more materials, often metals or a combination of metal and metal oxides, that are inert under standard conditions until subjected to a sufficiently strong stimulus [1,2]. The composition of a reactive material can be tailored to produce a desired energetic response, and often includes aluminum as the fuel source that oxidizes and converts chemical into thermal energy. Reactive materials can be ignited under high velocity impact loading conditions to produce a dust-debris cloud that reacts to produce high thermal energy [3]. While there are many studies on aluminum particle combustion in various flow environments [4], fewer studies investigate the thermal response of aluminum fragment oxidation in debris fields ignited by an impact event. Investigating thermal energy conversion and dissipation upon reaction induced by high velocity impact conditions is critical to optimizing properties of reactive materials for tailored ballistic applications.

A common experimental technique to study reactive material impact events uses a high-velocity gun-launched projectile into an instrumented catch chamber [5,6]. These systems provide the high dynamic loading conditions required to induce projectile fragmentation and reaction. *Postmortem* analysis of recovered materials from a ballistic impact experiment often includes X-ray diffraction (XRD) for species identification, analyses of fragment particle size distribution, and microscopy for evaluation of fragment morphology. This data provides an indication of energy conversion (e.g., thermochemical and kinetic energy) upon target penetration, impact and fragmentation. Another approach for quantifying energy conversion includes *in-situ* temperature measurements during the impact event. Temperature measurement technologies have recently become mature enough to incorporate into ballistic experiments. For example, optical measurement techniques have been successfully demonstrated for the high temperatures associated with aluminum particle combustion [7] and extended to explosive fireball studies to determine detonation temperatures on the microsecond timescale [8] that impose similar constraints as

* Corresponding author.
E-mail address: michelle.pantoya@ttu.edu (M.L. Pantoya).

https://doi.org/10.1016/j.ijheatmasstransfer.2022.122565
0017-9310/

ballistic environments. The goal of this study is to extend current ballistic research by adding temperature measuring diagnostics to evaluate thermal energy resulting from a reactive material projectile impact event.

Recent progress has been made in the modification of readily available high-speed cameras that allow for thermographic imaging [9,10]. Previous work characterized the limitations and advantages of both pyrometry and thermography for visualization of combustion phenomena during thermite reactions [11]. Densmore et al. [12] added thermography to a ballistic experiment to visualize a spatial distribution of temperature throughout the impact event. They used nickel aluminum (NiAl) and aluminum polytetrafluoroethylene (Al+PTFE) reactive material projectiles and measured reaction temperatures of 3600 K (NiAl) and 3300 K (Al+PTFE). More commonly, researchers [13] integrate point source measurement techniques such as pyrometry into ballistic experiments. Coupling these two energy measuring technologies offers tremendous potential for resolving energy conversion and dissipation in complex reactive flow fields.

The goal of this work is to measure thermal energy associated with ballistic impact events by combining and comparing two techniques: pyrometry and thermography. The objective is to use four-color pyrometry and high-speed thermographic imaging to characterize the transient temperature behavior of two different types of reactive material projectiles. The first projectile is identified as an intermetallic composed of a mixture of two metals, aluminum (Al) and zirconium (Zr). The second projectile is identified as a thermite composed of a mixture of a metal with a metal oxide; aluminum and molybdenum trioxide (MoO_3). These two formulations are commonly used in reactive material applications [14,15] and provide an opportunity to assess the two complementary detection techniques in terms of response time and range of temperature gradients measured. Results show the energy conversion process from these two formulations is very different and demonstrates that reactive materials can be designed to exhibit different fragmentation patterns which lead to different dispersions of thermal energy. These two formulations are not intended to categorize reactive materials into two designated behaviors, but instead illustrate the canvas of possibilities for tailoring thermal response in ballistic applications.

2. Experimental

2.1. Materials

Both reactive material projectiles were prepared by Matsys, Inc. (Sterling, VA). The intermetallic consisted of Al:Zr at a 30:70 mass ratio and the thermite consisted of Al:MoO_3 at a 60:40 mass ratio. All precursor powders were spherical with average diameter ranging from 10–15 µm. Powders were consolidated via hot isostatic pressing (HIP) using a proprietary processing protocol. Following sintering to 98% of their theoretical maximum density (TMD) by HIP, cylindrical pellets were produced by electrical discharge machining (EDM) of the consolidated billets. Further material analysis of the composite post-HIP processing is reported by Shancita et al. [16]. Cylindrical pellets of both materials were prepared with diameter and length dimensions of 0.95 cm. The pellets were placed into a nylon jacket sabot supported underneath by a nylon wad with the shot cup removed (model n. SG410, Ballistic Products Inc.) and loaded into a 0.410 bore shotgun shell hull (model no. 1394176, Ballistic Products Inc.) along with 1.7 g of shotgun propellent (Blue Dot, Alliant Powder) to achieve velocities of 1250 m/s. More details on projectile preparation and loading are provided in Cagle et al. [17].

2.2. High-velocity impact-ignition testing systems (HITS)

The High-Velocity Impact-Ignition Testing System (HITS) is a powder gun and catch chamber system designed for laboratory ballistics testing and shown in Figure. The chamber has polycarbonate windows (Makrolon AR2, McMaster-Carr) that allow multiple diagnostics to visualize the impact event and the ensuing combustion cloud. Three projectiles of each material were launched into the chamber at 1250 m/s so that three sets of temperature data for each projectile could be processed.

After launch, projectiles impacted a 2.54 cm thick A36 steel witness plate located in the rear of the chamber (Figurea). The chamber was instrumented with multiple diagnostics including pyrometry, thermography, and UV–VIS-NIR spectroscopy. The green shaded region and red shaded circle in Figureb indicate the fields of view for the thermographic high-speed camera (Phantom v710, Vision Research) and the 12 mm collimator (RC12SMA-P01, ThorLabs) used to collect light for the thermographer and pyrometer, respectively. The divider plate located 14.4 cm from the rear of the chamber has a 3.81 cm diameter hole aligned with the projectile flight path so that the projectile does not penetrate the plate prior to impacting the witness plate. The plate effectively reduces the chamber volume to the field of view of the thermography system.

2.3. Thermography

A high-speed color camera was modified for thermographic imaging. The Bayer color filter array on the camera sensor separates light into red, green, and blue partitions providing pixel level color intensity information [9]. Two infrared (IR) short-pass filters (675 nm and 725 nm) along with a triple-bandpass filter (633 nm, 533 nm, and 451 nm, 10 nm FWHM) were placed in front of the camera lens (24–70 mm EXDG, Sigma) to modify the optics so a local cluster of pixels behaves like a three-color pyrometer [18]. Camera acquisition settings were set to 66,000 fps for a 15.15 µs temporal resolution, and a spatial resolution of 160 × 304 pixels with an exposure time of 1.5 µs and an aperture f/2.8 on the lens. Additional filtering was achieved by implementing intensity thresholds in processing software to remove under and over saturated pixels. The camera's field of view encompasses a 14.4 × 27.4 cm section of the chamber illustrated by the green shaded region in Fig. 1b.

2.4. Pyrometry

A four-color pyrometer, described previously, was used to determine impact temperatures of both the thermite and intermetallic projectiles [11]. Light from the projectile impact was collected with a 12 mm collimator mounted to the side of the catch chamber, aligned with the witness plate center (Fig. 1b). Light was transmitted from the collimator to the pyrometer through a fanout optical fiber (200 µm, BF2LS01, ThorLabs), with the center fiber connected to the pyrometer. The fanout fiber and collimator assembly were used to simultaneously supply light to a spectrometer. Data acquisition was achieved using an oscilloscope (Picoscope, 5442A, Pico Technology) that provided a temporal resolution of 10 µs.

2.5. Temperature calculations

Pyrometry is defined as the derivation of temperature from radiant emission applying Planck distribution predictions [19]. The Planck distribution represents the maximum amount of radiation emitted by a diffuse blackbody (Eq. (1)).

$$I_b(\lambda, T) = \frac{C_1}{\lambda^5\left(\exp\left(\frac{C_2}{\lambda T}\right) - 1\right)} \quad (1)$$

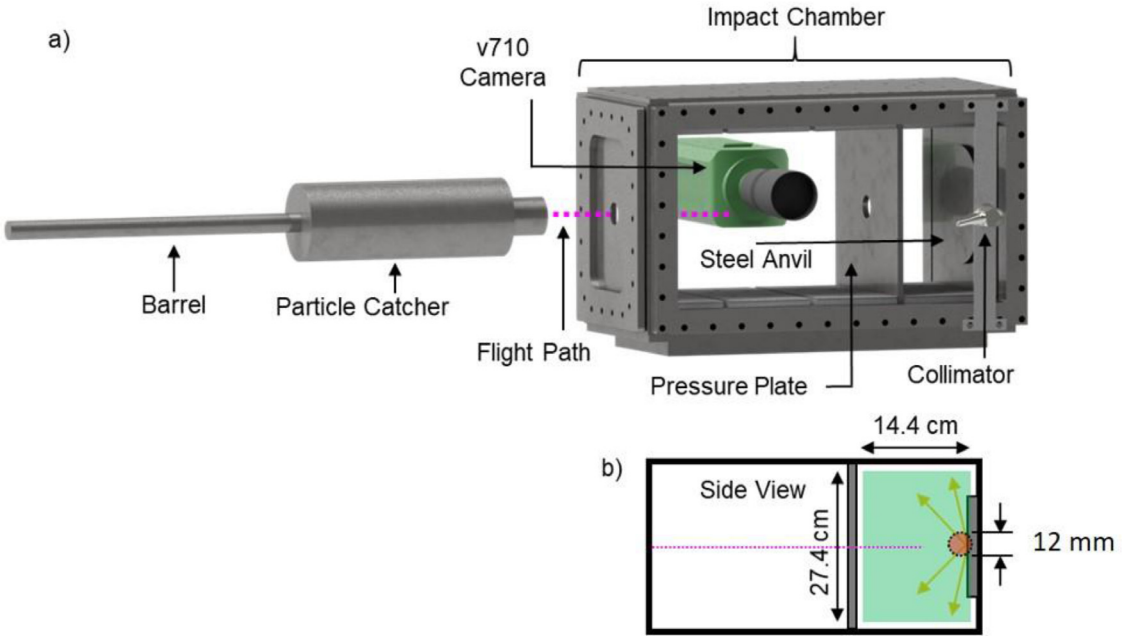

Fig. 1. a) Schematic of HITS apparatus with barrel aligned to the catch chamber. b) Side view of the catch chamber with green shaded region representing the cameras field of view and the red shaded circle representing the pyrometer field of view through a 12 mm collimator. Flight path of projectiles indicated by purple line in both schematics.

At shorter wavelengths (i.e., in the visible region) Wien's spectral distribution, a simplification of Planck Law, can be used in place of Planck's Law (Eq. (2)) [20,21]. Wien's spectral distribution is commonly used in pyrometry measurements due to its accuracy within 1% of Planck's Law predictions at combustion temperatures (2500 – 4500 K) [22].

$$I_b(\lambda, T) = \frac{C_1}{\lambda^5\left(\exp\left(\frac{C_2}{\lambda T}\right)\right)} \tag{2}$$

However, real surfaces emit at a fraction of the radiation emitted by a blackbody, therefore an assumption needs to be made about emissivity (ε), the efficiency of a surfaces ability to emit like a blackbody at wavelengths of interest (λ) (Eq. (3)).

$$I(\lambda, T) = \varepsilon\ I_b(\lambda, T) \tag{3}$$

For combustion applications, specifically aluminum combustion, there are three common assumptions made regarding emissivity. The first is the gray body assumption where emissivity is considered constant across wavelengths and therefore the collected radiative intensity is proportional to a blackbody [22]. The second assumes emissivity varies with wavelength inversely proportional to the specific wavelength (λ^{-1}) and the third similarly assumes wavelength varies with emissivity but with a λ^{-2} relationship [8]. A study by Kalman and Hedman [23] investigated the legitimacy of these assumptions when analyzing aluminum combustion temperatures. When aluminum oxide combustion clouds are optically thick, Kalman and Hedman showed the gray body assumption more accurately estimates emissivity. At later stages of a reaction, when more condensed phase alumina species begin to form and the cloud thins, they show a λ^{-2} assumption for emissivity is more applicable [24,23].

Because uncertainty is a complicated parameter to define for these instruments, varying the functional form of the emissivity is a useful method to interpret temperature calculations. As highlighted by Idrici et al. [13], the thermal emission signatures from ballistic impact can be described in two stages: stage-one occurs immediately upon impact, followed by stage-two that includes fragmentation, dispersion, and combustion of the debris field. When the projectile impacts the witness plate, the opacity of the combustion cloud coincides with a gray body assumption for emissivity. We have followed a similar methodology applied to the pyrometer data focused on the impact event. At later times, as the reacting material disperses and spreads throughout the chamber, the emissivity of the dispersion varies proportional to λ^{-2} as described by Kalman and Hedman [23] and better represents the thermography data. Woodruff et al. [25] showed that the temperature resulting from these varied emissivity assumptions can range by as much as 1000 K and is an inherent source of uncertainty in the analysis of temperature.

Manipulating Eq. (2) allows temperature to be extracted as the slope of the linear relationship between wavelengths and corresponding collected intensities shown in Eq. (4) [22]. Substituting Eq. (3) into Eq. (4) results in Eq. (5), where temperature is a function of collected raw intensity, emissivity, and wavelength.

$$T = \frac{C_2/\lambda}{\ln C_1 - \ln \lambda^5 I_b} \tag{4}$$

$$T = \frac{C_2/\lambda}{\ln C_1 - \ln \lambda^5 I/\varepsilon} \tag{5}$$

For the specific emissivity assumption of λ^{-2}, Eq. (5) takes the form of Eq. (6). Temperature calculations for thermography were performed using Eq. (6) for every pixel in each frame of high-speed video data and follow a similar multi-spectral radiation thermometry model as described by Weng et al. [26].

$$T = \frac{C_2/\lambda}{\ln C_1 - \ln \lambda^7 I} \tag{6}$$

2.6. Calibrations

Calibration factors ($x = measured/published$) were derived for both the pyrometer and thermographic camera using a tungsten-halogen lamp (SLS201L, ThorLabs). A lamp source is a cost-effective way of producing combustion temperatures (2500 – 4500 K) needed for calibrating the temperature measurement diagnostics [27]. The additional complexity of the high-speed thermographic camera requires further calibration steps to account for sources of error such as emission overlap between neighboring pixels. Pixel

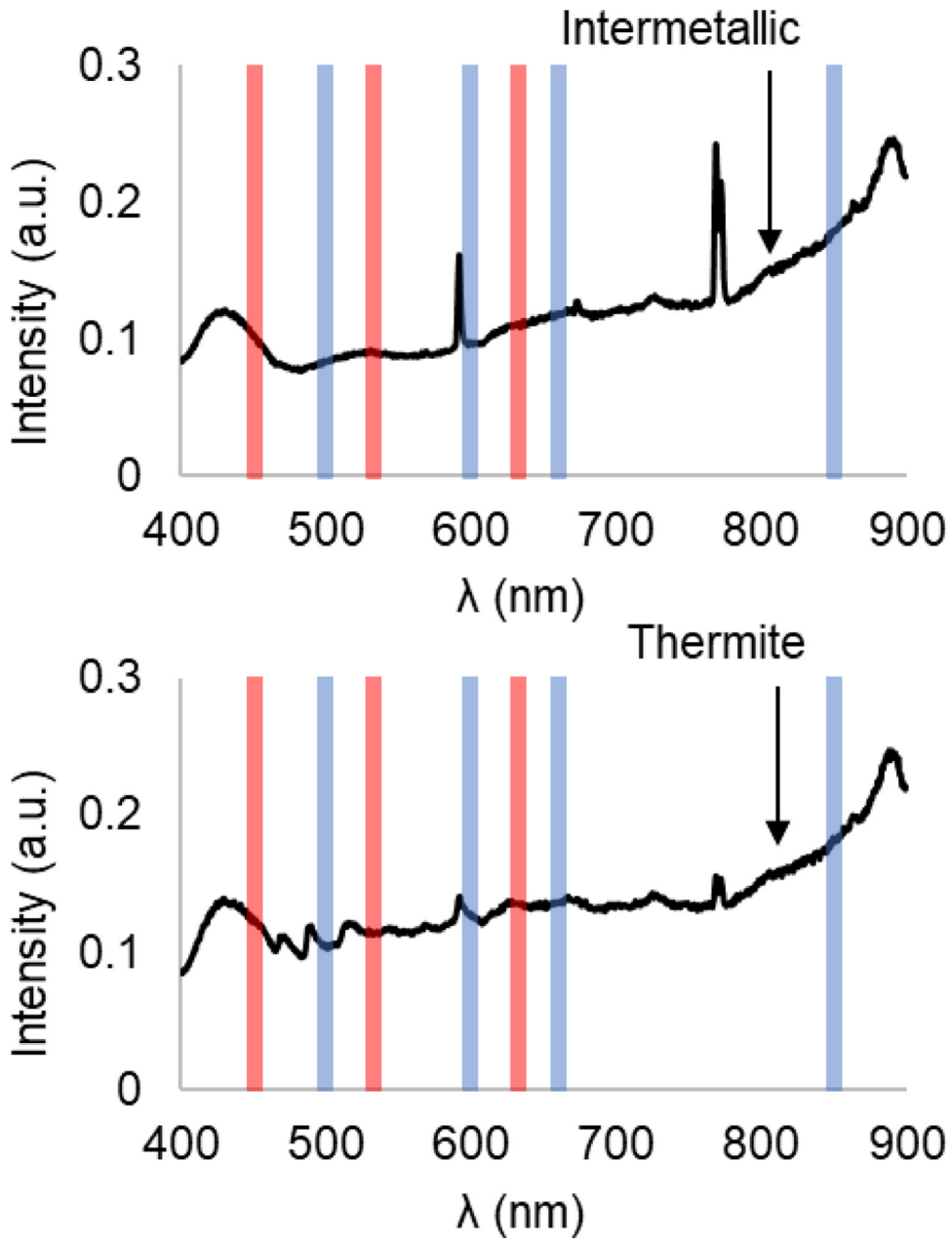

Fig. 2. Spectra from the intermetallic (top) and thermite (bottom) projectile impacts with blue bars representing pyrometer bandpass wavelengths and red bars representing the camera triple bandpass filter values.

correction factors were achieved using equations developed by McNesby et al., by directing monochromatic 625 nm and 530 nm light-emitting diodes (LEDs) into the camera [18]. Further details on the calibration process are described in previous work [11,25].

2.7. Spectroscopy

In order to ensure the reaction produces no emissions at wavelengths of interest that would cause error in temperature calculations, spectra from both the intermetallic and thermite projectiles were captured. Representative spectra collected by a UV–VIS-NIR spectrometer (200–1025 nm, Insight FX-XR1, Ocean Optics) at an integration time of 825 µs are illustrated in Figure. Along with the spectra, bars representing wavelengths monitored by the pyrometer (blue) and thermographic camera (red) are plotted.

In Fig. 2, two of the filtered regions raise concern for interference. The first is the 500 nm channel for the thermite. This channel intersects with the tail of a peak at 480 nm that is associated with AlO emission [28]. However, temperature calculations including this channel reported no erroneous temperature measurements that would raise concern. Additionally, the r-squared values collected from the linear temperature extraction in Eq. (5) never fell below 98%, suggesting limited AlO emission at 480 nm. The other concern arises from the camera's 451 nm bandpass channel. For both the intermetallic and thermite, an emission peak can be observed at 430 nm, as shown in Fig. 2. In this case, temperatures reported when using all three channels of the camera's triple-bandpass filter resulted in unrealistic temperatures and r-squared (R^2) values as low as 73%. Thus, camera-based temperature calculations were performed using data from the 633 nm and 533 nm channels only. While the data in Fig. 2 is useful for identifying wavelengths of concern, these data should be used with caution. The spatially and temporally integrated spectrum does not always capture the transient features of interest that can be

suppressed by the mostly thermal continuum of hot condensed phases.

3. Results and discussion

3.1. Flame temperature simulations

Measured flame temperatures were compared to theoretical values for the intermetallic and thermite reactions using thermal equilibrium simulations. The calculations were performed using thermochemical equilibrium software CHEETAH [29] and applying a constant pressure assumption. Simulations indicate theoretical maximum temperatures in excess of 4500 K and 4000 K for the intermetallic and thermite, respectively and provide a threshold for anticipated temperature measurements.

3.2. Thermography

Temperatures calculated for each frame of high-speed video are reported in Fig. 3(a) and (b). In order to represent the data more clearly, a moving average was performed to reduce the total data down to 100 points. Standard deviations determined through this averaging are shown with the maximum (red) and minimum (blue) data surrounding the average (black) temperature data in Fig. 3(a) and (b). The temperatures are reported per frame and plotted as a function of time. Also reported is the normalized intensity of the 633 nm channel for each frame (Fig. 3c). The thermite (solid line) emitted at a higher intensity than the intermetallic (dashed line). The thermite and intermetallic intensities in Fig. 3(c) were normalized to the maximum intensity reported for the thermite to better compare the dramatic difference in light emission.

Fig. 3 shows that both the thermite and intermetallic projectiles react upon impact and burn at similar temperatures, with averages around 2800 K. This is an interesting result and suggests that for both the intermetallic and thermite, the average flame temperature may be best represented by aluminum oxidation that is molecularly abundant in both materials. However, the intermetallic has a larger standard deviation with upper limits consistent with the higher AFT anticipated from the intermetallic reaction simulation. The multiple reaction pathways for the intermetallic projectile include metal oxidation but also intermetallic reactions may be the cause of the higher standard deviation than for the single metal-based thermite reaction.

The intermetallic data has an inflection around 150 ms where the signal to noise ratio decreases resulting in inaccurate peak temperatures beyond 150 ms. The thermite data shows a similar inflection, but at a later time (i.e., 250 ms). The inflection represents a transition in burning behavior, resulting from diminished light intensity (Fig. 3c). As the reaction begins to extinguish, the signal to noise ratio appreciably decreases [11]. Fig. 3c confirms the intermetallic emission intensity plateaus past 150 ms, coinciding with the inflection in peak temperature from Fig. 3a. Further illustrated in Fig. 3c is that at 250 ms, thermite intensity data approaches the intermetallic, consistent with decreased signal-to-noise as reactions extinguish.

Still frames and calculated thermographic images for both the intermetallic and thermite projectiles are shown in Fig. 4. Frames were selected at arbitrary time stamps to highlight interesting behaviors in the combustion clouds. The brightness and contrast of the raw images were increased for illustrative purposes. The last frames from Fig. 4 show that emission from both materials considerably decays and confirms that low emission causes error in temperature measurements (see late times in Fig. 3).

Fig. 4 illustrates the difference in thermal performance between the two projectiles. Previous groups have shown that metal-based reactive material projectiles release a majority of their energy after the projectile fragments and experiences secondary impacts with the chamber walls [30]. The secondary impacts cause ignition, observed in the still frames of the intermetallic, specifically in the frames captured at 4.21 ms and 7.85 ms. At these two times, intermetallic particles rebound and impact the plate (right side of image) and re-impact the witness plate (left side of image). Note the brightness intensifies at the edges of the frame, corresponding with edges of the plate and witness plate. Further, at later stages of combustion (e.g., 130 ms and 318 ms), hot particles can still be observed lingering within the chamber.

The thermite is primarily aluminum combustion with some solid oxidizer, so increased gas generation is expected compared to the intermetallic [31]. This increased gas generation is evident in frames 0.30–28.95 ms (Fig. 4), where more chamber volume is occupied by hot combustion gasses. Further, unlike the intermetallic projectile, the thermite produces a combustion cloud that expands throughout the chamber quickly after impact. Visual and thermal images of the cloud expansion are shown in the first three still frames of Fig. 4 all occurring within 0.67 ms of impact. The unique thermal data compared in Fig. 4 from both intermetallic and thermite materials indicate that even under high impact dynamic loading conditions, materials can be selected for specific thermal responses.

3.3. Pyrometry

The pyrometer is more effective at capturing the large temperature variations seen directly post-impact due to its enhanced dynamic range when compared to the thermographic camera system [25]. The fiber collimator captures light centered at the witness plate to observe the projectile impact event. Applying Eq. (5) with a gray body assumption to the pyrometer data results in representative temperature curves for intermetallic and thermite combustion, shown in Fig. 5. The high r-squared values resulting from the temperature curve fit to Eq. (5) (blue curve) and the low standard deviation (shaded gray region) at the early stages of data collection (i.e., $<$ 100 ms) indicate reliable temperature calculations. From 100 ms onward, the standard deviation increases, and the r-squared values fluctuate, attributed to the diminishing light from the reaction, represented by the normalized intensity data from the 850 nm channel (green curve). However, even with the larger standard deviations, temperatures are still below the AFT from simulations.

Fig. 5a shows intense emission upon impact followed by a drop coincident with a momentary decrease in temperature. Similarly, the still frame images of Fig. 4 indicate high emission upon impact followed by a drop for several ms duration. The video data in Fig. 4 complement the pyrometry data in Fig. 5a and elucidate that the intermetallic releases significant thermal energy after the fragments experience secondary impacts with the chamber walls [30].

Fig. 5b shows the thermite temperature at impact, but with a shorter timescale. The shortened timescale is due to the thermite reaction quickly expanding away from the witness plate and out of the pyrometer's field of view. In the thermal data, the expansion outside the pyrometer's field of view manifests as an increase in standard deviation and a fluctuation of the r-squared value after $\sim$ 1 ms, corresponding with the drop in reported 850 nm channel intensity. The temperatures average $\sim$ 3800 K until 1.2 ms, where the standard deviation begins to exceed theoretical AFT for the thermite. These measured peaks remain within 200 K of theoretical AFT. The average trend in temperature between 1.2–2 ms fluctuates around the 3800 K temperatures seen earlier in the data.

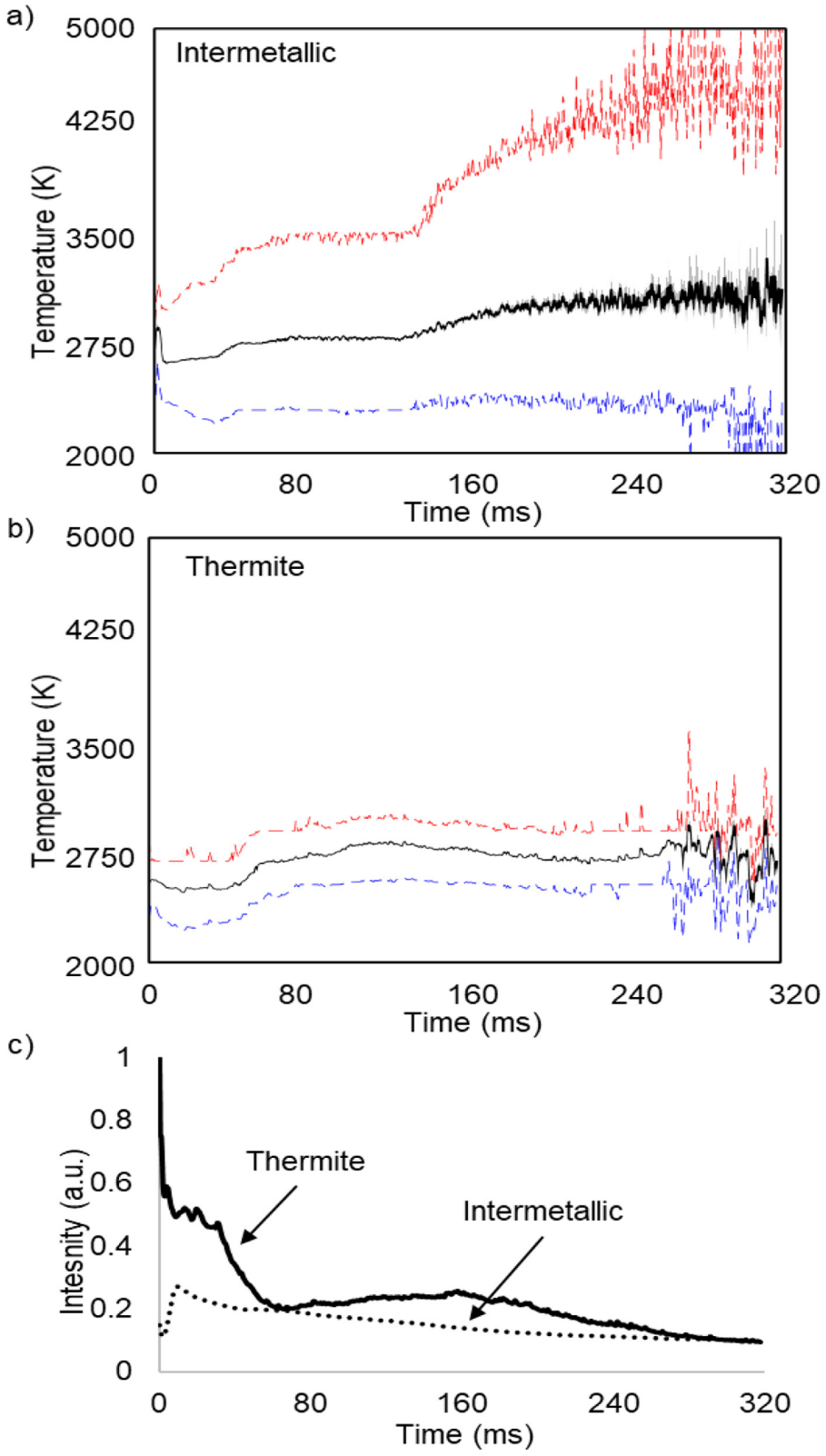

Fig. 3. a) Intermetallic data from thermographic high-speed video with maximum (red), minimum (blue), and average (black) temperatures reported for each frame. b) Thermite data from thermographic high-speed video with maximum (red), minimum (blue), and average (black) temperatures reported for each frame. c) Normalized intensity from 633 nm channel for each mixture, note that data were normalized to maximum intensity reported by the thermite due to higher intensity for that material. (For interpretation of the references to color in this figure legend, the reader is referred to the web version of this article.)

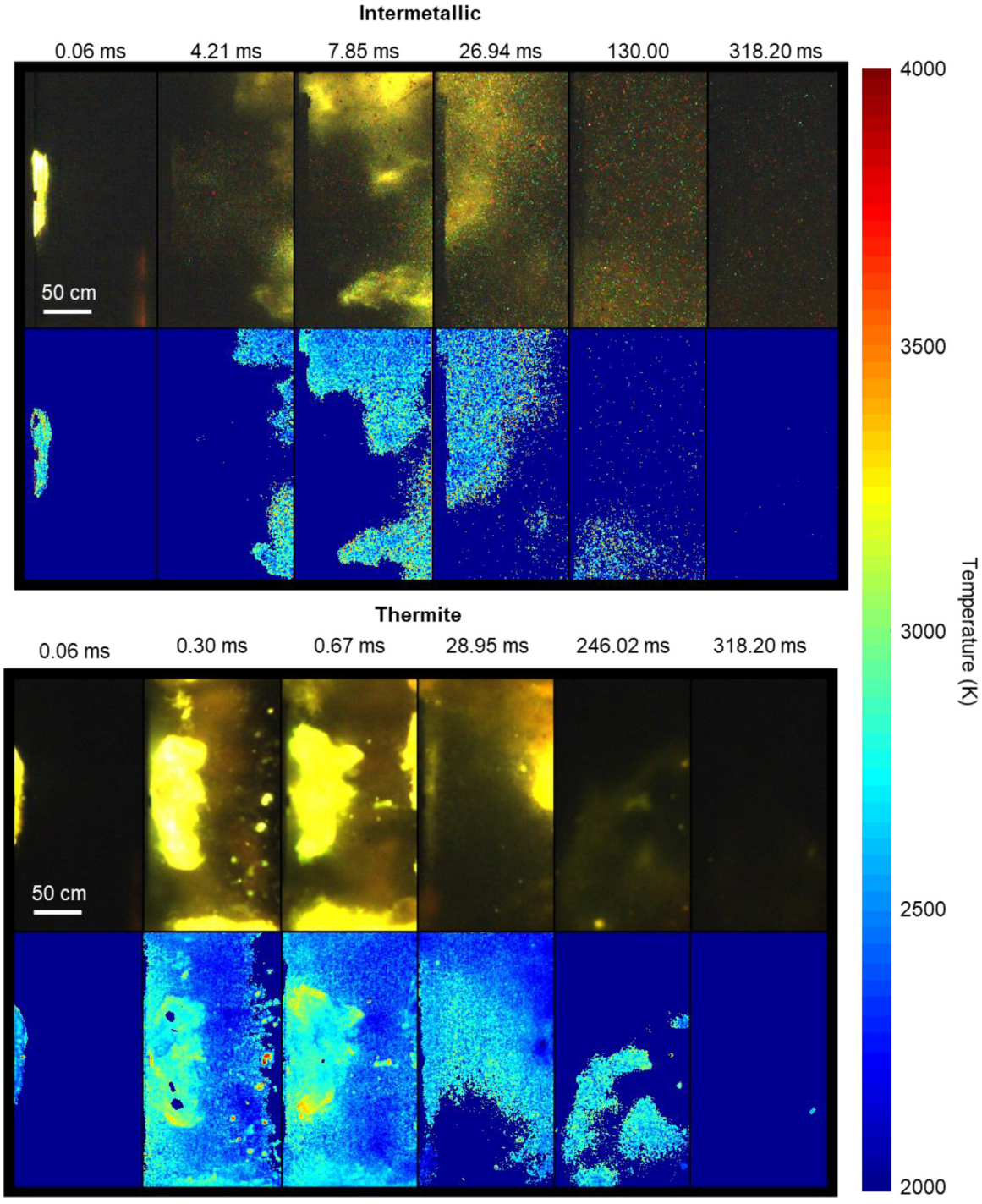

Fig. 4. Still frame and reconstructed thermographic images of the intermetallic (top) and the thermite (bottom) at selected times during combustion event. Projectile impact velocities are 1250 m/s. Note that frames from different times are shown for the two impacts.

3.4. Dissipation

An advantage to incorporating high-speed thermographic imaging with ballistic applications is the ability to obtain information on thermal dissipation rates. By quantifying how many pixels are reporting a temperature for each video frame, an area can be calculated indicating spatial variations within the chamber containing hot particles. Because the area is determined as a function of time, the dissipation rate defines the rate at which the area affected by hot particles cools. While this method provides a spatial understanding of thermal dissipation, the analysis is two-dimensional, and the depth variations associated with a three-dimensional asymmetrical cloud would need multiple camera perspectives to fully realize.

Calculations were performed for both materials from high-speed videos and the resulting thermal dissipation curves are presented in Fig. 6. Distinct features in the dissipation curves are noted with corresponding still frame images visualizing these features. Thermal dissipation rates provide a supplementary perspective of behavior beyond the temperature graphs in Fig. 3.

A linear fit was applied to the shaded green region between 50 and 180 ms in Fig. 6a for the intermetallic projectile, providing a

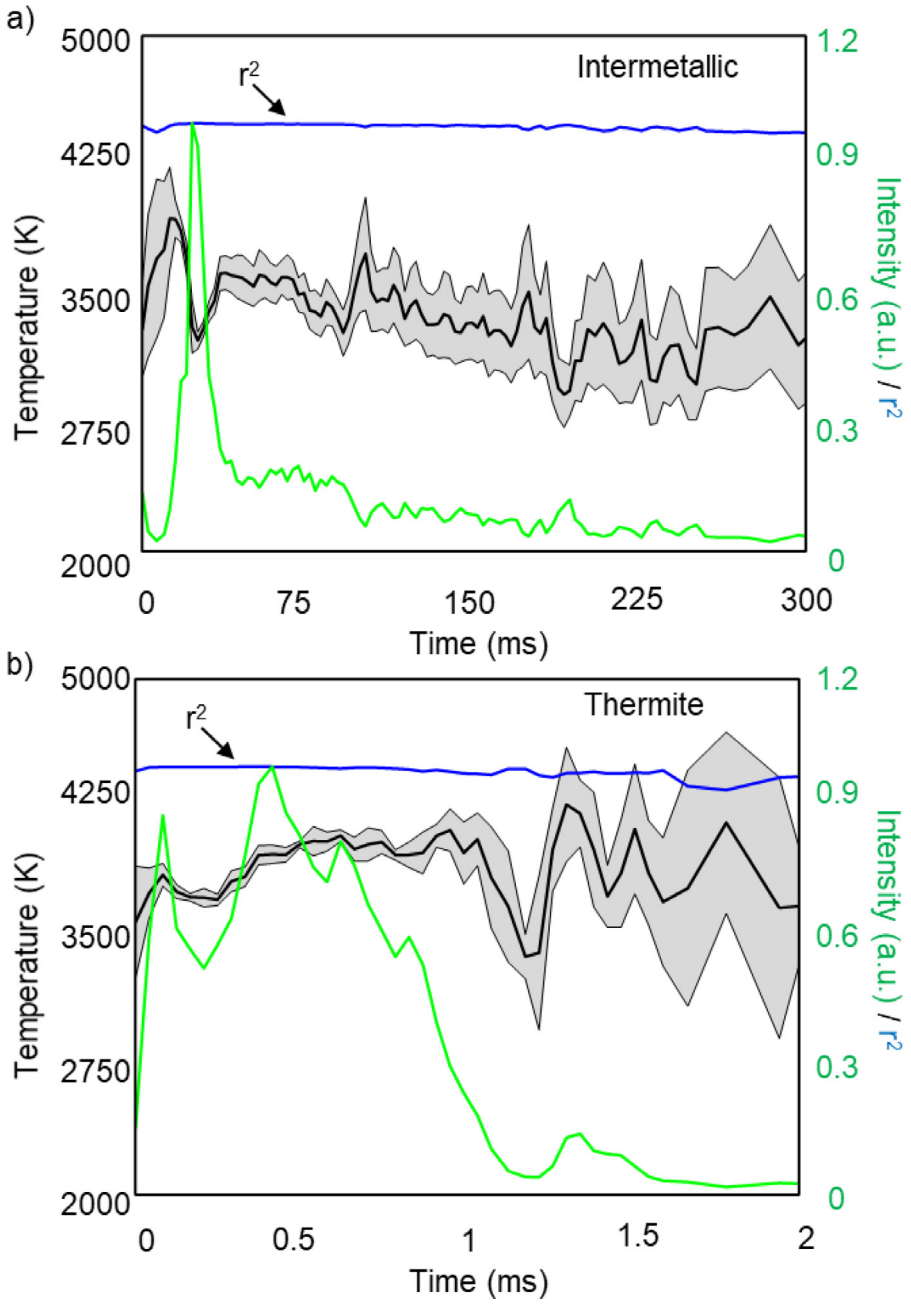

Fig. 5. Pyrometry data for the intermetallic (a) and thermite (b) with average temperature (black curve), standard deviation (gray shading) and normalized intensity data from the 850 nm channel (green curve).

dissipation rate of 0.9 cm^2/ms. Fig. 6b shows that the intermetallic particle cloud remains suspended in the chamber, therefore a low dissipation rate in Fig. 6a is reasonable. The dissipation curve of the thermite in Fig. 6c follows more of a stochastic trend because the thermite reaction is more dependent on convective gas flows than the reaction associated with the intermetallic projectile. The stochastic behavior is attributed to sintered particles propelled around the chamber, in and out of the field of view of the camera. Additionally, fragment micro-explosions within the combustion cloud are observed. These micro-explosions can be seen in Fig. 6d in the first still frame as large bright points enclosed in the green boxed regions. Other notable features present in Fig. 6c include a steep drop to a low point labeled as point 4 and then an increase in reported temperatures up to point 5. This phenomenon is attributed to the fragments settling in the bottom of the chamber (Fig. 6d: 71.05 ms), but as combustion continues hot gasses rise back up into the camera field of view (Fig. 6d: 208.00 ms). The only section of the curve that can be analyzed as steady dissipation is the green shaded region between 200 and 270 ms with a rate of 3.1 cm^2/ms.

3.5. Particle fragment analysis

The high-speed thermographic imaging system also allows investigation of discrete burning particles. The high spatiotemporal abilities of the camera inherently allow particle tracking. By modifying the high-speed visual imaging for thermography, it is possible to monitor both particle position and temperature. This capability is illustrated in Fig. 7 where a representative frame from the thermite reaction is analyzed. Four particles (A-D) are tracked,

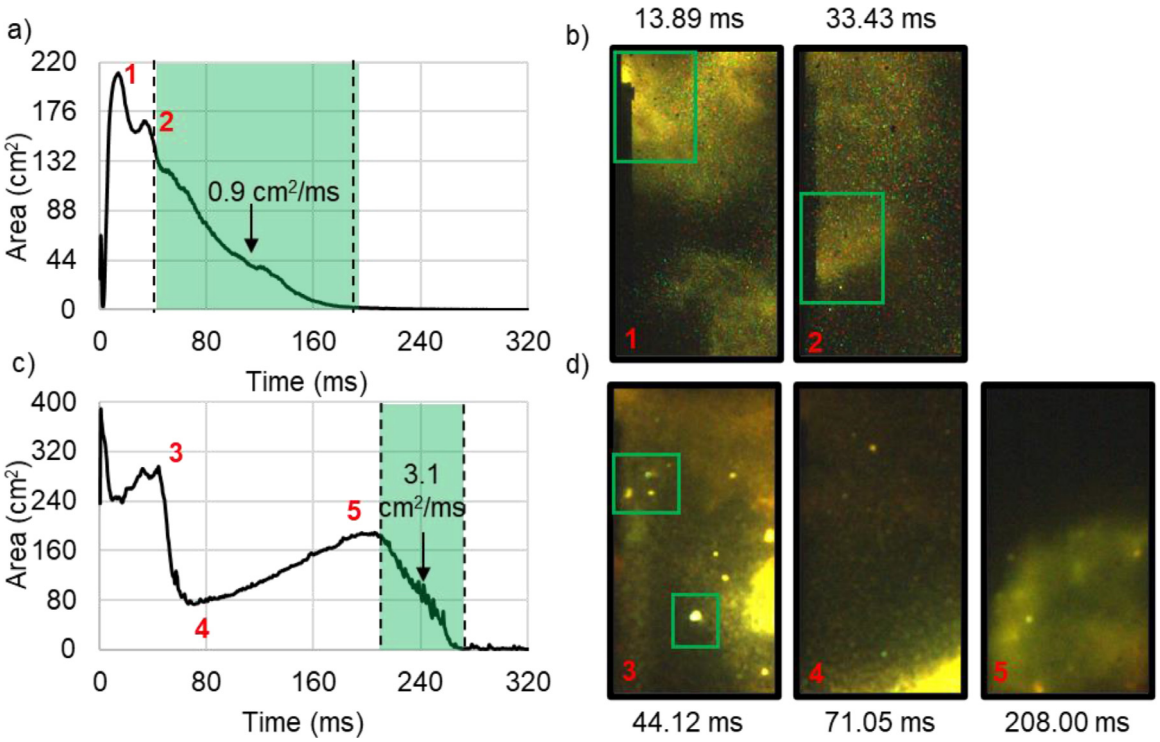

Fig. 6. Dissipation curves of the (a) intermetallic impacts with a dissipation rate calculated for the green shaded region and (b) frames of interest numbered in red. (c) Thermite impacts with a dissipation rate calculated for the green shaded region and (d) frames illustrating behavior of dissipation curve numbered in red on the plot and corresponding image frames. (For interpretation of the references to color in this figure legend, the reader is referred to the web version of this article.)

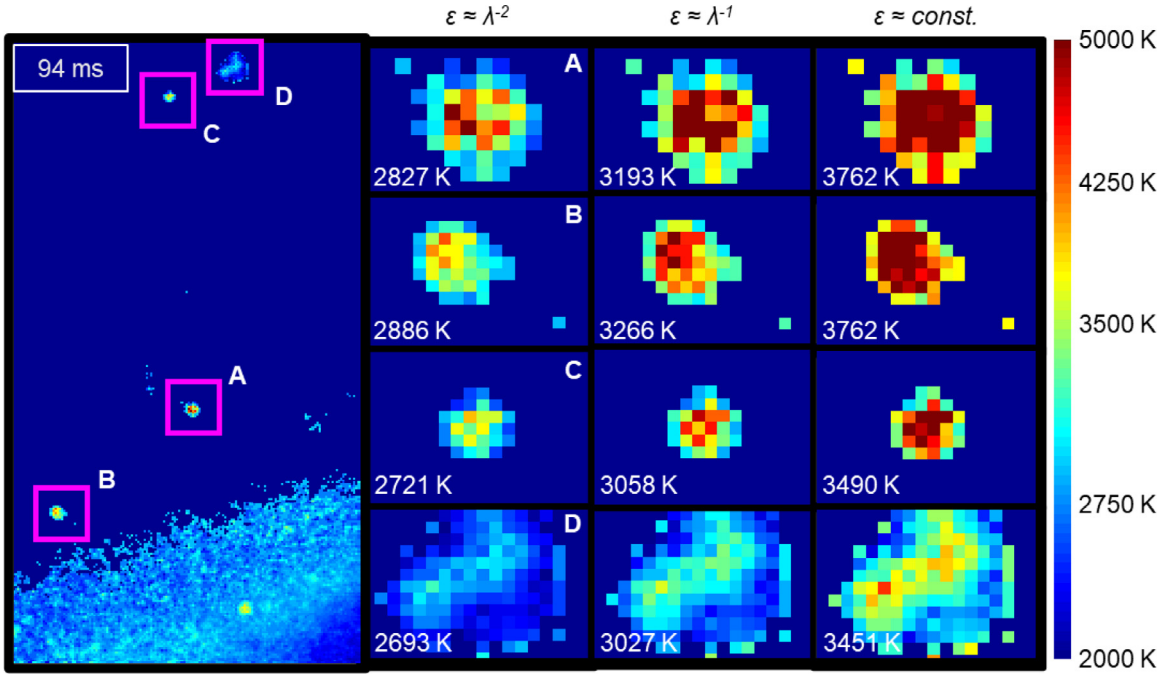

Fig. 7. Thermographic image from the thermite impact with particles A-D extracted and average temperatures reported. Temperature calculations were performed with different emissivity assumption shown from left to right.

and average temperatures are reported. Additionally, to emphasize the influence that emissivity assumption has on calculated temperatures, the three common emissivity assumptions previously discussed were applied (i.e., $\varepsilon \approx$ const., $\varepsilon \approx \lambda^{-1}$, and $\varepsilon \approx \lambda^{-2}$).

The particles in Fig. 7 are likely oxidizing aluminum, as the reported temperatures are consistent with aluminum combustion [27]. Looking at the enlarged particle images, it is evident that thermographic analysis grants fine spatial detail of the transient temperature behavior of these particles. Each pixel seen in the images represents a 0.9 × 0.9 mm spatial area. Further, to affirm correct selection and importance of emissivity assumption, ranging emissivity values were applied for agglomerate temperature analysis. The temperatures vary by almost 1000 K between emissivity assumption. When applying a gray body assumption (i.e.,

$\varepsilon = 1$, third column in Fig. 7), the particles report temperatures near 3800 K, approaching AFT calculations.

4. Discussion

Thermite and intermetallic projectiles were launched into a steel witness plate in the back of a catch chamber at $\sim$ 1250 m/s. Both pyrometry and high-speed thermography were implemented to resolve thermal behavior during the impact, fragmentation, and reaction events. Results indicate that both materials burn at similar temperatures at impact and during reaction.

Impact temperatures reported by the pyrometer were calculated under the gray body assumption resulting in temperatures between 3500 K and 4000 K (Fig. 5) for both materials. The post-impact intermetallic fragments linger within the chamber for a significant amount of time. In contrast, the thermite violently disperses and spreads away from the pyrometer field of view, located at the anvil impact site.

Thermographic high-speed videos indicate both materials have an average reaction temperature around 2800 K (Fig. 4). As previously mentioned, a λ^2 assumption was applied for emissivity treatment to compensate for the much larger and spatially resolved field of view of the camera where combustion products spread out more thinly throughout the chamber. For aluminum heating a similar emissivity assumption was previously established to show the highest accuracy in temperature prediction for both oxidized and unoxidized aluminum [26]. The intermetallic reported peak temperatures of 3500 K and the thermite reported 3000 K. This is to be expected considering the intermetallic contains zirconium, a much hotter burning metal. The average temperatures are similar likely because aluminum oxidation dominates for most of the reaction.

Though the materials perform similarly from a temperature perspective, the temperatures are generated by different mechanisms. The intermetallic exhibits temperature increases associated with fragments from secondary impacts, a feature previously reported with intermetallic reactive materials. As fragments rebound around the chamber, newly formed intense areas are observed in still frame images while corresponding spikes are observed in the number of pixels reporting temperatures for those time intervals (Fig. 6b). The thermite burns with a more stochastic nature as the material quickly produces hot particulates and gasses throughout the chamber (Fig. 6a). Additionally, micro-explosions of fragmented particles are observed with the thermite. Fig. 7 shows average agglomerate temperatures range from 2700–2900 K, consistent with aluminum oxidation. The differences in thermal behavior and propagation of combustion between the intermetallic and thermite while producing similar temperature regimes highlights the potential of these materials for different ballistic applications.

For the thermite, there is significantly more post-impact gas generation than the intermetallic. The thermite includes MoO_3, a gas generating solid oxidizer, however the thermite is almost entirely aluminum with very little solid oxidizer relative to the fuel. Zhang [32] explains that MoO_3 may facilitate reaction by providing interface discontinuities that promote fragmentation and aluminum particle combustion through hot spot formation. Furthermore, aluminum particle combustion is a vapor phase process when reacting with oxygen gas from the environment. Vapor phase aluminum will envelope a burning particle, creating a gap between the flame and the condensed phase droplet [33]. This burning process is multi-phase, whereas zirconium oxidation occurs in the condensed phase [34]. Additionally, zirconium is a refractory metal and zirconium and zirconium oxide have sublimation temperatures sufficiently high to absorb the entirety of the oxidation energy without vaporizing. Specifically, the sublimation point of both zirconium metal and zirconium oxide is above 4500 K, which is greater than the temperatures produced in these reactions. Therefore, vapor phase species are more likely in the thermite reaction than in the intermetallic. The differences in combustion and thermal behavior between the intermetallic and thermite, while also producing similar temperatures, highlight the potential of these materials for different applications.

5. Conclusion

Combining pyrometry and thermography provides more complete insight into the thermal behavior of the impact event. While the pyrometer is more accurate at evaluating temperature at the initial impact due to its enhanced dynamic range, it lacks spatial resolution and is constrained to measuring temperatures within a narrow field of view. High-speed video analysis has been a common diagnostic in characterizing energetic material reactions but incorporating thermography into ballistic applications is more novel. The combination of the high spatial and temporal resolution from high-speed video, alongside temperatures at locations and times of interest, provides useful insight into the thermal performance of different reactive materials in ballistic applications.

The intermetallic reported peak temperatures of 3500 K and the thermite reported 3000 K. The intermetallic fragments linger within the chamber while the thermite violently disperses upon impact. The intermetallic contains zirconium, a much hotter burning metal and increases the peak measured temperature beyond the thermite. The average reaction temperatures for both materials are 2800 K and similar because aluminum oxidation dominates for most of the reaction.

Though the materials perform similarly from a temperature perspective, the temperatures are generated by different mechanisms. The intermetallic exhibits temperature increases associated with fragments from secondary impacts. For the thermite, there is significantly more gas generation than the intermetallic and burning appears more stochastic as the material produces hot particulates and gasses throughout the chamber with micro-explosions of fragmented particles. The differences in combustion and thermal behavior between the intermetallic and thermite, while also producing similar temperatures, highlight the potential of these materials for different applications.

Data availability

The data that support the findings of this study are available from the corresponding author upon reasonable request.

Declaration of Competing Interest

All authors declare no conflicts of interest.

CRediT authorship contribution statement

Connor Woodruff: Conceptualization, Investigation, Formal analysis, Writing – original draft. **Steven W. Dean:** Investigation, Methodology, Formal analysis, Writing – original draft. **Colton Cagle:** Investigation. **Charles Luke Croessmann:** Investigation. **Pascal Dubé:** Resources, Conceptualization. **Michelle L. Pantoya:** Conceptualization, Supervision, Writing – original draft.

Acknowledgements

We are thankful for partial support from the Army Research Office (Grant W911NF1710387), the Office of Naval Research (Grant N000141912082, STEM Grant N000142112519), and the U.S. Department of Energy (STEM Grant DE-NA0003988). Additionally, Sandia National Laboratories is a multi-mission laboratory managed

and operated by National Technology & Engineering Solutions of Sandia, LLC, a wholly owned subsidiary of Honeywell International Inc., for the U.S. Department of Energy's National Nuclear Security Administration under contract DE-NA0003525. This paper describes objective technical results and analysis. Any subjective views or opinions that might be expressed in the paper do not necessarily represent the views of the U.S. Department of Energy or the United States Government.

References

[1] Committee On Advanced Energetic Materials and Manufacturing TechnologiesAdvanced Energetic Materials, National Research Council, Washington DC, 2004.
[2] J. Yang, S. Wang, H. Chen, Effect of interface thermal resistance on ignition of reactive material by a hot particle, *Int. J. Heat Mass Transf.* 97 (2016) 146–156.
[3] M. Beason, I. Gunduz, S. Son, The role of fracture in the impact initiation of Ni-Al intermetallic composite reactives during dynamic loading, *Acta Mater.* 133 (2017) 247–257.
[4] M. Bidabadi, S. Biouki, E. Yaghoubi, A. Rouboa, A. Poorfar, M. Mohebbi, Reaction-diffusion fronts of aluminum dust cloud in a system of random discrete sources, Energy 107 (2016) 639–647.
[5] R. Ames, in: Energy Relase Characteristics of Impact-Initiated Energetic Materials, 308, MRS Online Proceedings Library, 2006.
[6] R. Ames, Vented chamber calorimetry for impact-initiated energetic materials, AIAA 279 (2005).
[7] Y. Feng, Z. Xia, L. Huang, L. Ma, Effect of ambient temperature on the ignition and combustion process of single aluminum particles, Energy 162 (2018) 618–629.
[8] P. Lynch, H. Krier, N. Glumac, Emissivity of aluminum-oxide particle clouds: application to pyrometry of explosive fireballs, *J. Thermophys. Heat Transf.* 24 (2) (2010) 301.
[9] J.M. Densmore, M.M. Bliss, K.L. McNesby, B.E. Homa, High-speed digital color imaging pyrometry, *Appl. Opt.* 50 (2011) 2659–2665.
[10] K. McNesby, S. Dean, R. Benjamin, J. Grant, J. Anderson, J. Densmore, Imaging pyrometry for most color cameras, *Rev. Sci. Instrum.* In Press (2021).
[11] C. Woodruff, S. Dean, M. Pantoya, A comparison of pyrometry and thermography for thermal analysis of thermte reactions, *Appl. Opt.* 60 (16) (2021) 4976–7985.
[12] J. Densmore, M. Biss, B. Homan, K. McNesby, Thermal imaging of nickel-aluminum and aluminum-polytetrafluoroethylene impact initiated combustion, *J. Appl. Phys.* 112 (2012) 084911.
[13] D. Idrici, S. Goroshin, M. Soo, D. Frost, Light emission signatures from ballistic impact of reactive metal projectiles, *Int. J. Impact Eng.* 150 (2021) 103814.
[14] D. Stamatis, E. Dreizin, K. Higa, Thermal initiation of Al-MoO_3 nanocomposite materials by different methods, *J. Propuls. Power* 27 (5) (2011) 1079–1088.
[15] E. Wainwright, S. Dean, S. Lakshman, T. Weihs, J. Gottfried, Evaluating compositional effects on the laser induced combustion and shock velocities of Al/Zr-based composite fuels, *Combust Flame* 213 (2020) 357–368.
[16] I. Shancita, C. Cagle, I. Kalish, P. Dube, J. Abraham, B. Hammond, J. Warzywoda, M. Pantoya, Tailoring thermal transport properties by inducing surface oxidation reactions in bulk metal composites, *ACS Appl. Mater. Interfaces* (2021).
[17] C. Cagle, K. Hlll, C. Woodruff, M. Pantoya, J. Abraham, C. Meakin, Target penetration and impact analysis of intermetallic projectiles, *Int. J. Impact Eng.* 136 (2020) 103427.
[18] K.L. McNesby, S.W. Dean, R. Benjamin, J. Grant, J. Anderson, J.M. Densmore, Imaging pyrometry for most color cameras, *Rev. Sci. Instrum.* (2021) Pending.
[19] S. R. Turns, An I**ntroduction** to Combustion, McGraw-Hill, New York, NY, 1996.
[20] H. Orlande, O. Fudym, D. Mallet, R. Cotta, Thermal Measurements a**nd** Inverse T**echnique**s, CRC Press, Boca Raton, FL, 2011.
[21] A. Araujo, Mult-spectral pyrometry - a review, Meas. Sci. Technol. 28 (2017).
[22] D. Dagel, G. Grossette, D. MacCallum, S. Korey, Four-color imaging pyrometry for mapping temperatures of laser based metal processes, in: Proceedings of SPIE: Thermosense: Thermal Infrared Applications, 38, 2016.
[23] J. Kalman, T. Hedman, On the origin and use of the emissivity approximations for alumina particles, Propellants Explos. Pyrotech. 41 (2016) 793–797.
[24] J. Kalman, D. Allen, N. Glumac, H... Krier, Optical depth effects on aluminum oxide emissivity, J. Thermophys. Heat Transfer 43 (2015) 74–82.
[25] C. Woodruff, S.W. Dean, C. Cagle, C.L. Croessman, M.L. Pantoya, Pyrometry and thermography in ballistic impact expirements, Measurement (2021) 110488.
[26] K.-H. Weng, C.-D. Wen, Effect of oxidation on aluminum alloys temperature prediction using multispectral radiation thermometry, *Int. J. Heat Mass Transf.* 54 (2011) 4834–4843.
[27] S. Fischer, M. Grubelich, Theoretical Energy Release of Thermites, Intermetallics, and Combustible Metals, 1998 Sanida National Laboratory Technical Reports SAND98-1176CAlbequerque.
[28] J.L. Gottfried, E.J. Bukowski, Laser-shocked energetic materials with metal additives: evaluation of chemistry and detonation performance, *Appl. Opt.* 56 (3) (2016).
[29] L. Fried, P. Souers, CHEETAH: aA Next Generation Thermochemical Code, 1994 Lawrence Livermore National Laboratory Technical Report No. UCRL-ID-117240Livermore, CA.
[30] D. Bohl, R. Lee, Study of the break-up and impact of a metal/polymer composite material in a two-step process, International Annual Conference-Fraunhofer Institut fur Cheische Technologie, 11, 2006.
[31] B. Bockmon, M. Pantoya, S. Son, B. Asay, J. Mang, Combustion velocities and propagation mechanisms of meta-stable intermolecular composites, J. Appl. Phys. 98 (6) (2005) 064903.
[32] F. Zhang, Some issues for blast from sturctural reative material solid, Shock Waves 28 (2018) 693–707.
[33] I. Altman, On energy accommodation coefficient of gas molecules on metal surface at high temperatures, *Surf. Sci.* 698 (2020) 121609.
[34] M. Arimondi, U. Anselmi-Tamburini, A. Gobetti, Z. Munir, G. Spinolo, Chemical Mechanism of the $Zr + O_2$->ZrO_2 Combustion Synthesis Reaction, J. Phys. Chem. B 101 (1997) 8059–8068.